Title:

CLASSIFICATION OF AXISYMMETRIC SHAPES OF DROPLETS ON FIBERS. COULD NON-WETTABLE FIBERS SUPPORT AXISYMMETRIC DROPLETS?

Authors:

Yueming Sun(孙悦鸣), 515 Calhoun Drive, 161 Sirrine Hall, Dept. of Materials

Science and Engineering, Clemson University, Clemson, SC 29634, USA

Alexander V. Bazilevsky, Ishlinsky Institute for Problems in Mechanics of the

Russian Academy of Sciences, Moscow 119526, Russia

Konstantin G. Kornev, 515 Calhoun Drive, 161 Sirrine Hall, Dept. of Materials

Science and Engineering, Clemson University, Clemson, SC 29634, USA

kkornev@clemson.edu

Abstract: With the developments in nanotechnology, nanofibrous materials attract great attention as possible platforms for fluidic engineering. This requires an understanding of droplet interactions with fibers when gravity plays no significant role. This work aims to classify all possible axisymmetric configurations of droplets on fibers. The contact angle that the drop makes with the fiber surface is allowed to change from 0° to 180° . Nodoidal

apple-like droplets with inverted menisci cusped toward the droplet center and unduloidal droplets with menisci cusped away from the droplet center were introduced and fully analyzed. The existing theory describing axisymmetric droplets on fibers is significantly enriched introducing new morphological configurations of droplets. It is experimentally shown that the barreled droplets could be formed on nonwettable fibers offering contact angles greater than 90°. The theory was quantitatively confirmed with hemispherical droplets formed at the end of a capillary tube and satisfying all the boundary conditions of the model. It is expected that the developed theory could be used for design of nanofiber-based fluidic devices and for drop-on-demand technologies.

1 Introduction

Since childhood, droplets of water or glue on spider webs[1-3] and needle-like leaves[4-6] have captured people's attention. These observations make us wonder how a drop could find its perfect symmetric shape and stay unperturbed for a long time. These shapes are not only aesthetically attractive but practically important. Droplets on fibers are of great interest for inspiration and development of novel fiber-based microfluidics ranging from fiber-based liquid collectors and fabric-based filters to the fluid delivery devices[2, 7-10].

The drop shape significantly depends on the wetting properties of materials. In everyday life, one would think about a flat substrate as wettable by the given liquid if a

drop would make contact angle less than 90° with it. Otherwise, a flat substrate would be considered non-wettable, implying that the drop could be easily shaded off from it. This 90° contact angle criterion for wettable surfaces is practically attractive but not necessarily correct as it comes to the condition of drop detachment[11, 12].

Therefore, the analyses of conditions of wetting and dewetting of flat surfaces received the deserved attention from physicists and materials scientists, and the 90° contact angle criterion was corrected to include different physicochemical characteristics of substrates [11, 13, 14].

One cannot say the same about fibers. Wetting of fibers remained poorly understood and offers many surprises calling for a special approach in the classification of fiber wettability [8, 15-20].

Take, for example, a low surface tension oil, which would readily wet a flat surface and spread over it, forming a puddle, Fig. 1(a) [11]. However, oil would not form a sheath analogous to a 2D puddle on a fiber made of the same material. When the drop volume is small, the drop may form an asymmetric clamshell, Fig. 1(b), (d). And when the volume is large, the drop forms an axisymmetric barrel-like drop, Fig. 1(c), (e). The analysis of this clamshell-barrel transformation has been rigorously studied, yet a clear picture of the mechanism of this transformation has yet to emerge [8, 17-19, 21-26].

Surprisingly, unlike flat substrates, where a spherical cap is the basic drop configuration in the absence of gravity, only one spherical drop could meet the fiber at the given contact angle, Fig. 1 (f-g). For this spherical drop, the radius $R_{\emptyset} = \frac{R_f}{\cos \theta}$ is fully

determined by the contact angle θ and the fiber radius R_f . To allow the change of the drop volume, one has to consider some other droplet shapes. This makes the problem of surface characterization of fibers very difficult as one has first to determine the drop shape and only after that calculate the contact angle.

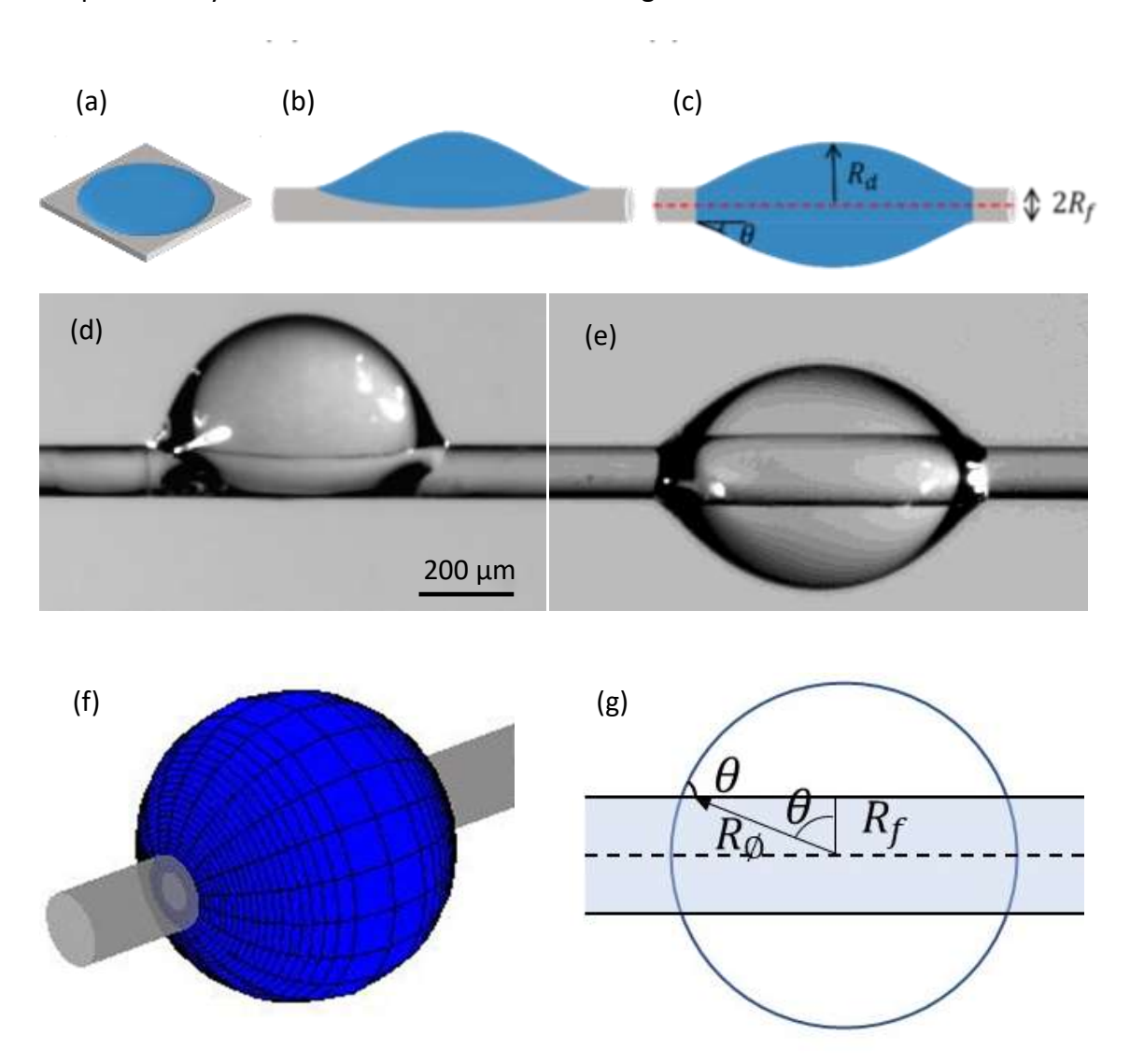


Fig. 1. (a) A drop of a wetting liquid spreads on a flat surface. On a fiber made of the same material, the same drop may form either a clamshell drop (b) or a barreled drop (c). The shape of the

barreled drop with its maximum radius R_d is controlled by the contact angle (θ) , the fiber radius R_f and the droplet volume. (d) Side view of clamshell and (e) barreled water drops sitting on a nylon fiber with a diameter of $2R_f=100~\mu m$. (f) The drop may form a sphere if and only if the contact angle (θ) , the fiber radius R_f and the drop radius are related as $R_{\emptyset}=\frac{R_f}{\cos\theta}$. All these parameters are defined in (g).

Joseph Plateau was, probably, the first to rigorously study the spontaneous formation of the barreled droplets on fibers; his research inspired Lord Rayleigh, who studied dynamic phenomena associated with this process[27, 28]. The phenomenon of the inherent instability of cylindrical liquid bodies has been named after Plateau and is known as the Plateau instability. D'Arcy Wentworth Thompson found very many applications of this fundamental work to biology[29]. Since then, the spontaneous formation of droplets by fibrous materials has attracted attention of biologists and engineers[1, 15-17, 30-32].

While the Plateau instability received great attention from fluid mechanicians and materials scientists [33, 34], a rigorous classification of axisymmetric shapes of droplets on fibers is lacking. Yet, it is in high demand [8, 18-20, 23, 24]. Carroll[35] postulated that the profiles of the barreled drops must be described by unduloids[36, 37], a family of constant mean curvature surfaces.

Surprisingly, to the best of our knowledge, the other family of constant mean curvature surfaces, nodoids[36, 37], has never been investigated. This family of solutions becomes important as the fiber size decreases to micrometers and below micrometers, and the effects of droplet weight diminish. For example, one can think about aerosol

droplets captured by a nanofiber in a filter and question whether a non-wettable fiber could capture and hold such a drop. To answer this question, consider a drop with the surface tension σ resting on a fiber. The energy (per unit surface area of the fiber) required to detach the droplet from the fiber is equal to the work of adhesion $W_{adh} = \sigma(1+\cos\theta)$. This energy is always finite unless $\theta=180^\circ$. Thus, the droplet is always attracted to the fiber, and one can assume that the large droplets would be able to wrap up the non-wettable fiber with $\theta>90^\circ$. These arguments motivated us to study all possible shapes of axisymmetric droplets on fibers, assuming that gravity is unimportant.

We investigated nodoidal and unduloidal droplets and determined the transition from one family to another. The critical radius R_{\emptyset} serves as a characteristic scale for the problem as it naturally couples the fiber radius with the contact angle characterizing the wetting properties of fibers. We use this characteristic radius in our analysis by scaling the drop sizes. It is shown that the Carroll choice of unduloidal droplets has its limitations. To describe all possible wetting scenarios, one needs to include nodoidal droplets. Nodoidal droplets significantly enrich the family of barreled axisymmetric droplets. The fibers could be completely wrapped up by these droplets even if the droplets make contact angles greater than 90° . We attempted to validate the theory experimentally and confirmed that the nodoidal apple-looking droplets with inverted menisci could be observed in experiments at predictable conditions.

2 Equilibrium shapes of droplets on fibers

2.1 Laplace law for axisymmetric droplets

The equilibrium droplets have constant pressure P^- everywhere inside the liquid body. The difference between P^- and pressure P^+ in the surrounding fluid is defined by the Laplace law of capillarity as[36-39]:

$$P^- - P^+ = \sigma \left(\frac{1}{R_r} + \frac{1}{R_g} \right) \tag{1}$$

where R_r and R_g are the two principal radii of curvature, and σ is the interfacial tension between phases. In applications to axisymmetric droplets on fibers, the two principal radii of curvature at an arbitrary point A on the drop surface are introduced in Fig. 2.

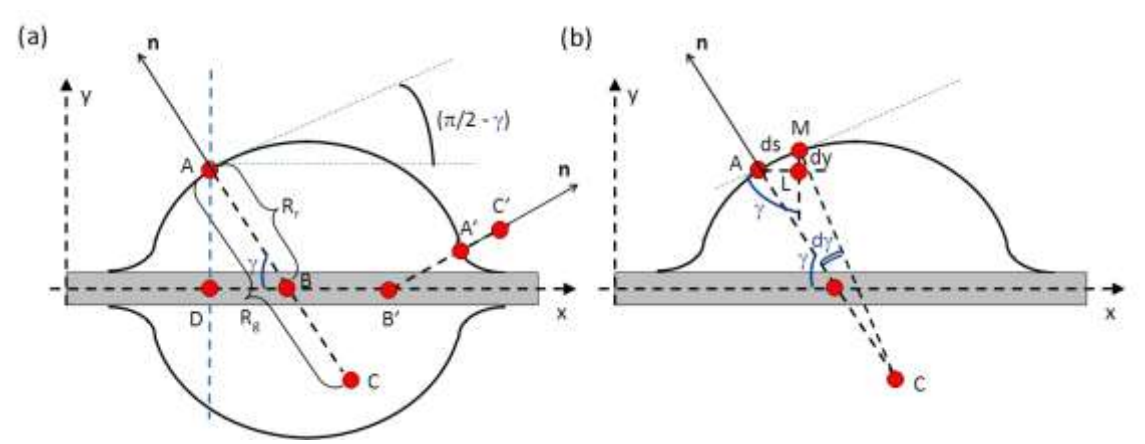


Fig. 2. Schematic illustrating the principal radii of curvature calculated at point A on the droplet surface. The first principal radius of curvature $R_g=AC$ in Fig. 2(a) is merely the curvature of the plane curve AA'. The center of curvature C lies on the ray AB passing through the outward normal vector \mathbf{n} . The curvature of the plane curve AA' is found as $1/R_g=d\gamma/ds$, where angle γ is defined as the angle that the ray AB makes with the axis of symmetry \mathbf{x} ; \mathbf{s} is the arc length along the generator curve AA'. The relation between the incremental change of $d\gamma$ and ds as the

observer moves from point A to point M along the generator AA' is derived using the schematic in Fig. 2(b). The second principal radius of curvature R_r is obtained by continuing the ray AB along the normal vector ${\bf n}$ until it intersects the fiber axis at point B in Fig. 2(a). Noticing that the angle $\widehat{DBA}=\gamma$ of the right triangle ADB is related to the inclination angle $\pi/2-\gamma$ formed by the tangent at point A with the x -axis, one can relate $|AB|=R_r$ with the drop radius y at point A as $R_r=y/\sin\gamma$. For point A, pinned to an egg-like surface patch, both centers of principal curvatures, C and B, are found inside the drop; the curvatures are defined as positive. For point A' pinned to a saddle-like surface patch, the centers of curvatures C' and B' are separated by the generator AA'; therefore, one curvature is positive, and the other is negative with respect to the ${\bf n}$ direction. For example, when the drop wets the fiber completely, making zero contact angle, an infinitesimally small patch on the meniscus near the fiber looks like a saddle, and the curvature $1/R_r$, $|R_r|=|B'A'|$, is positive. Another curvature, $1/R_g$, $|R_g|=|A'C'|$, is negative.

The drop is obtained by rotating the generator, a plane curve AA', y=y(x), in Fig. 2, around the x-axis. Taking an arbitrary point A at the droplet surface and drawing the outward normal vector \mathbf{n} , we define the two principal radii of curvature, R_r and R_g by continuing the ray shown as the dashed line along the normal vector, Fig. 2. As explained in the figure caption, the two principal radii of curvature are defined as

$$R_g = |AC| = \frac{ds}{dv} \quad , \tag{2}$$

$$R_r = \frac{y}{\sin \gamma} \quad . \tag{3}$$

Turning to the right triangle AML and noticing that the angle \widehat{AML} in Fig. 2 (b) is equal to γ , and the side ML of this triangle is equal |ML|=dy, we have

$$ds = \frac{dy}{\cos \gamma}, \Longrightarrow \frac{1}{R_a} = \frac{d\gamma}{ds} = \frac{d\gamma}{dy} \frac{dy}{ds} = \frac{d\gamma}{dy} \cos \gamma.$$
 (4)

it is convenient to introduce dimensionless variables and new notations as

$$X = x\Delta P/\sigma$$
, $Y = y\Delta P/\sigma$, $S = s\Delta P/\sigma$, where $\Delta P/\sigma = (P^- - P^+)/\sigma$. (5)

Substituting Eqs. (3) and (4) into the Laplace equation Eq. (1) and using normalization (5), we obtain $1 = \frac{d\gamma}{d\gamma}\cos\gamma + \frac{1}{\gamma}\sin\gamma$, or

$$Y = Y \frac{d\gamma}{d\gamma} \cos \gamma + \sin \gamma. \tag{6}$$

2.2 Two families of the constant mean curvature surfaces and how to distinguish one from the other

Equation (6) can be integrated as follows. First, we notice the following identity $d(Y \sin \gamma) = Y \cos \gamma d\gamma + \sin \gamma dY$. Therefore, by dividing this differential by dY, one obtains

$$Y\cos\gamma\frac{d\gamma}{dY} = \frac{d\left(Y\sin\gamma\right)}{dY} - \sin\gamma,\tag{7}$$

Substituting Eq.(7) in Eq. (6), we have

$$Y = \frac{d(Y\sin\gamma)}{dY} - \sin\gamma + \sin\gamma,\tag{8}$$

After simplification, Eq.(8) is represented as $Y = \frac{d(Y \sin \gamma)}{dY}$, or

$$YdY = d(Y\sin\gamma). (9)$$

Integrating Eq.(9), one obtains the explicit solution

$$Y\sin\gamma = \frac{1}{2}Y^2 + C,\tag{10}$$

Where C is an integration constant. Equation (10) is quadratic with respect to Y. Hence it has two different solutions for a given γ . The real-valued solutions are determined by analyzing the discriminant $D=\sin^2\gamma-2C$. This straightforward analysis, Fig. 3(a), leads to the following conclusions.

All solutions of Eq. (10) are divided into two families, Fig 3 (b). When constant C varies between $0 \le C \le 1/2$, the surfaces of this family correspond to unduloids, Fig. 3 (c). When the constant C is negative C < 0, the surfaces of this family correspond to nodoids, Fig. 3 (e). These two families of constant mean curvature surfaces [37, 40] will be used to describe the drop configurations on fibers. We will distinguish these families by the integration constant C.

To plot these surfaces, the Laplace equation (1) is parameterized by the arclength S and rewritten as a set of the following first-order differential equations: $\frac{dX}{dS} = \sin\gamma \ , \\ \frac{dY}{dS} = \cos\gamma \ , \\ \frac{dY}{dS} = 1 - \frac{\sin\gamma}{Y}.$ For plotting these surfaces, we used the following initial conditions: $X(0) = 0, \gamma(0) = \pi/2$ and to find the initial condition for Y(0), we solved Eq.(10), $Y(0) = [Y(0)]^2/2 + C$ for the given C. Some examples of the 2D sections of these surfaces are shown in Fig. 3 (c, e) by first plotting the numerical solution

(X(S),Y(S)) and then using its mirror-symmetric image (X(S),-Y(S)) to show the boundaries of the enclosed area.

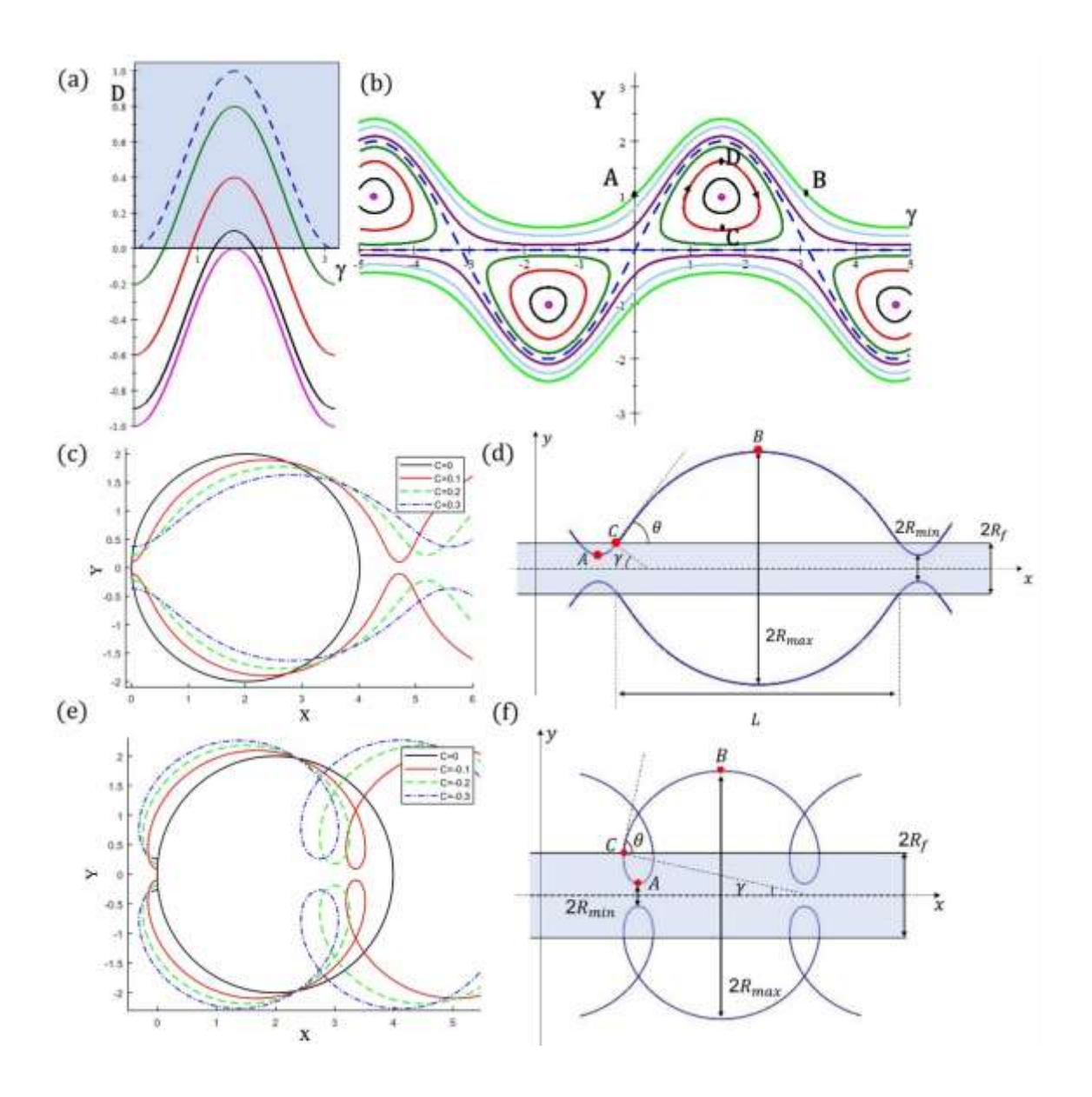


Fig. 3. (a) The behavior of discriminant $D=\sin^2\gamma-2C$ as a function of γ when the constant C is positive. The dashed blue curve corresponds to C=0; the green curve, C=0.1; the red curve, C=0.3; the black curve, C=0.45. In contrast to the other curves, the magenta curve

corresponding to C=0.5 touches the γ axis only at one point, $\gamma_s=\pi/2$. (b) The two different types of solutions to Eq.(10). The continuous curves propagating from negative to positive infinity without loops correspond to one family of solutions, the nodoids. The closed loops correspond to the other family of solutions, the unduloids. The dashed blue curve corresponds to C=0; the green curve, C=0.1; the red curve, C=0.3; the black curve, C=0.45; the discrete magenta dots correspond to, C = 0.5; the purple curve, C = -0.1, the Alice blue curve, C = -0.3; the light green curve, C = -0.5. (c) Unduloids are plotted for Y(0) = 0, 0.105, 0.225, 0.367, corresponding to C = 0, 0.1, 0.2, 0.3, respectively. Only one limiting circle (C=0) is shown. Observe how the neck diameter changes with the variation of these parameters. (d) Application of the unduloidal solutions for the description of droplets on fibers. In an unduloidal drop on a fiber of radius R_f , the neck of radius R_{min} is "hidden" inside the fiber. One can introduce the droplet radius as the maximum height of the unduloid bulge, R_{max} , and the contact angle θ at the contact line, point C. (e) Nodoids are plotted for Y(0) = 0, -0.0954, -0.1832, -0.2649 corresponding to C = 0, -0.1, -0.2, -0.3, respectively. Observe how non-physical knots form as one varies these parameters. (f) Application of the nodoidal solutions for the description of droplets on fibers. In a nodoidal drop on a fiber of radius R_f , the knot and the neck of radius R_{min} must be "hidden" inside the fiber. One can introduce the droplet radius as the maximum height of the nodoid bulge, R_{max} and the contact angle θ at the contact line, point C.

2.3 Unduloidal droplets

We assume that there is a unduloidal drop sitting on a fiber with radius R_f , and the drop forms contact angle θ with the fiber surface, Fig. 3 (d).

At the neck of the unduloid (point A in Fig. 3(d)), we have $\gamma=\frac{\pi}{2}$ and $y=R_{min}$. Therefore, Eq. (10) is written as

$$R_{min} = \frac{\Delta P}{2\sigma} R_{min}^2 + \frac{\sigma}{\Delta P} C. \tag{11}$$

At the bulge of the unduloid (point B in Fig. 3(d)), we have $\gamma=\frac{\pi}{2}$ at $y=R_{max}$. Therefore,

$$R_{max} = \frac{\Delta P}{2\sigma} R_{max}^2 + \frac{\sigma}{\Delta P} C. \tag{12}$$

Solving these two equations (11)-(12) for the pressure drop, we immediately obtain

$$\Delta P = \frac{2\sigma}{R_{max} + R_{min}}. (13)$$

Solving for constant C, we have

$$C = \frac{\Delta P R_{min}}{\sigma} - \frac{1}{2} \left(\frac{\Delta P}{\sigma}\right)^2 R_{min}^2 = \frac{2R_{max}R_{min}}{(R_{max} + R_{min})^2}.$$
 (14)

Since $R_{max} > R_{min} > 0$ in Eq. (13), the pressure drop in the unduloid is always positive suggesting that the pressure inside unduloid is always greater than the pressure in the surrounding fluid. Moreover, investigating Eq. (14), we confirm that the constant varies between $0 \le C \le 1/2$. As $R_{min} \to 0$, the unduloid transforms into a sphere, and the constant C goes to zero; as $R_{min} \to R_{max}$, the unduloid transforms into a circular cylinder, and the constant C goes to 1/2. Thus, Eq. (10) contains all possible unduloidal solutions.

2.4 Profile of unduloidal drop

We can apply the unduloidal solution (10) to describe the profile of the drop on fiber. In the general case of unduloidal solution, the neck of the unduloid describing the drop is invisible, Fig. 3(d). Therefore, to use Eq. (13) - (14) the neck radius has to be determined. We apply Eq. (10) to find it at the fiber surface where the drop meets the fiber at contact angle θ .

At the contact line between the unduloidal drop and fiber (point C in Fig. 3 (d)), we have $\gamma=\frac{\pi}{2}-\theta$ at $y=R_f$. Therefore,

$$R_f \sin\left(\frac{\pi}{2} - \theta\right) = \frac{\Delta P}{2\sigma} R_f^2 + \frac{\sigma}{\Delta P} C. \tag{15}$$

Solving Eq. (12) and Eq. (15) for pressure drop ΔP , we find the following expression

$$\Delta P = 2\sigma \frac{R_{max} - R_f \cos \theta}{R_{max}^2 - R_f^2} \tag{16}$$

Substituting Eq. (16) in Eq. (13), the neck radius of the unduloid can be rewritten in terms of observable parameters

$$R_{\min} = \frac{R_{\max}^2 - R_f^2}{R_{\max} - R_f \cos \theta} - R_{\max} .$$
 (17)

Similarly, C can be rewritten as,

$$C = \frac{2R_{max}R_f(R_{max} - R_f\cos\theta)(R_{max}\cos\theta - R_f)}{(R_f^2 - R_{max}^2)^2} .$$
 (18)

In order to ensure the existence of an unduloidal drop on fiber, we have to guarantee that the following conditions are met:

1) The neck radius of the unduloid must be positive and smaller than the fiber radius.

$$0 \le R_{\min} \le R_f, \Longrightarrow 0 \le \frac{R_{\max}^2 - R_f^2}{R_{\max} - R_f \cos \theta} - R_{\max} \le R_f \tag{19}$$

- 2) The bulge of the unduloid must be above the surface of the fiber, $R_f < R_{max}$.
- 3) In conditions 1-2, the contact angle θ is allowed to change from 0° to 90° ; therefore, $0 \le \cos \theta \le 1$.

Solving the left-hand side of the inequality (19) for R_{max} with constraints $R_f < R_{max} \ \& \ 0 \le \cos \theta \le 1$, we have

$$\frac{R_f}{\cos \theta} \le R_{max} \quad . \tag{20}$$

Solving the left-hand side of the inequality (19) for R_{max} , we have $\cos\theta \leq 1$, which holds. Thus, $R_f \leq \frac{R_f}{\cos\theta}$ holds. Thus, for the given contact angle θ that varies from 0° to 90° , we can always find an unduloidal drop. The maximum radius of this drop must be greater than the radius of the limiting sphere, $\frac{R_f}{\cos\theta}$.

2.5 Relation between the capillary pressure and the size of unduloidal droplets on fibers

The unduloidal drop of limiting radius $R_{max}=\frac{R_f}{\cos\theta}$ has a very special geometrical meaning. Substituting $R_{max}=\frac{R_f}{\cos\theta}$ in Eq. (18), we find C=0. This constant C=0 corresponds to the case when the unduloid turns into a sphere. Since $R_{max}=\frac{R_f}{\cos\theta}$ specifies the smallest possible radius of unduloidal drop, Eq. (20), this radius $\frac{R_f}{\cos\theta}$ sets up the boundary of the existence of unduloidal droplets on fibers. Below the curve $n=\frac{1}{\cos\theta}$ shown in Fig. 4 (b), no unduloidal droplets can exist.

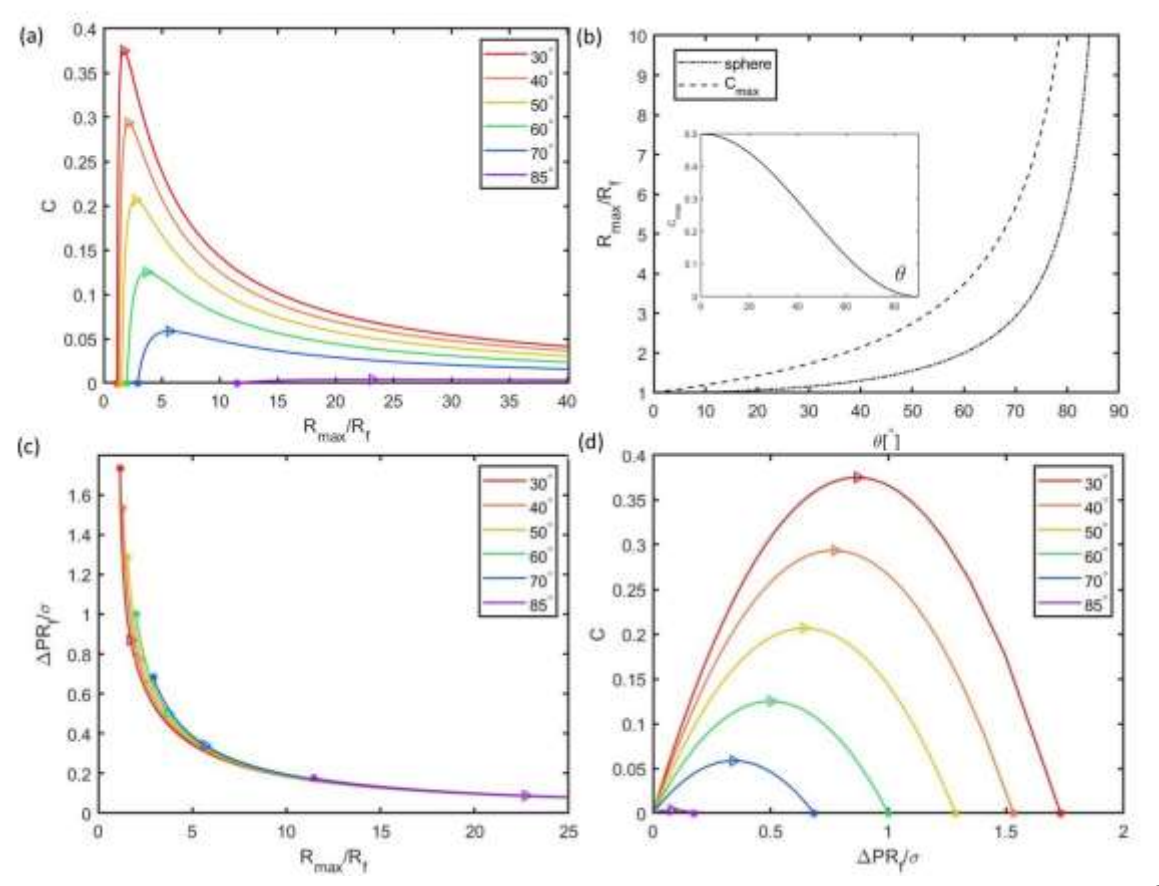


Fig. 4. (a) The dependence of constant C on the ratio R_{max}/R_f at different contact angles. The hollow triangles label the maximum values of C. The asterisks correspond to the spherical droplets of radius $R_{max} = \frac{R_f}{\cos\theta}$ meeting the fiber surface at the given contact angle θ . (b) The dashed curve specifies the boundary C_{max} where the maximum values of integration constant C, the hollow triangles in (a), have been reached. The critical ratio $\frac{R_{max}}{R_f} = \frac{1}{\cos\theta}$ specified by the dash-dotted curve corresponds to the boundary where the unduloidal drop becomes spherical. Below this curve, no unduloidal droplets can exist. The insert shows the dependence of C_{max} on the contact angle as follows from Eq. (23). (c) Dimensionless capillary pressure $\frac{\Delta PR_f}{\sigma}$ versus dimensionless radius of unduloidal drop $\frac{R_{max}}{R_f}$. (d) The constant C versus dimensionless capillary pressure $\frac{\Delta PR_f}{\sigma}$ versus to the maximums of C-curves. The asterisks correspond to the spherical droplets with the radius $R_{max} = \frac{R_f}{\cos\theta}$ and capillary pressure $\Delta P = 2 \cos\theta/R_f$.

As discussed earlier, the constant C fully specifies the shape of an unduloid. For an unduloidal drop on fiber, this constant is fixed by R_{max} , see Eq. (18). Therefore, we are able to investigate the dependence of C on R_{max} .

In Fig. 4(a), we plot C versus dimensionless drop radius R_{max}/R_f at different contact angles. Owing to constraint (20), each curve has a unique beginning point $R_{max}=R_f/\cos\theta$, asterisked in Fig. 4(a). Surprisingly, the plots show that constant C changes with the size of the unduloidal drop non-monotonously. Moreover, the maximum value

of C is not necessarily ½. The hollow triangles in Fig. 4(a) label the maximum peaks on each curve. This non-monotonous dependence suggests that each C selects not a single unduloid but two different unduloids with different R_{max} .

When R_{max} goes to infinity, C approaches zero as $C \approx \frac{2R_{max}R_f(R_{max})(R_{max}\cos\theta)}{(R_{max}^2)^2} = R_f\cos\theta/R_{max} \to 0$. Again, this constant C=0 corresponds to the case when the unduloid turns into a sphere. Thus, we have two limiting spheres, one has a finite radius $\frac{R_f}{\cos\theta}$, and another has an infinite radius.

The non-monotonicity of constant C on the maximum radius of unduloidal droplet calls for establishing a selection principle for the given unduloid as a possible model of a droplet resting on a fiber. Taking the partial derivative of C, Eq. (18), with respect to R_{max} , we analyze the dependence of the drop radius R_{max} corresponding to the maximum of C as a function of contact angle θ :

$$\frac{\partial C}{\partial R_{max}} = \frac{2R_f \left[\cos\theta \left(R_f^4 + 6R_f^2 R_{max}^2 + R_{max}^4\right) - R_f R_{max} (\cos 2\theta + 3) \left(R_f^2 + R_{max}^2\right)\right]}{\left(R_f^2 - R_{max}^2\right)^3}$$

$$= 0,$$

Or

$$\cos\theta (1 + 6n^2 + n^4) - n(\cos 2\theta + 3)(1 + n^2) = 0$$
, where $n = R_{max}/R_f$. (21)

Equation (21) has to be solved with constraints $0 < R_f < R_{max} \& 0 < \theta < \frac{\pi}{2}$. As shown in Supplementary materials, Eq.(21) has a unique solution:

$$n = \frac{1 + \sin \theta}{\cos \theta} \Rightarrow R_{max} = \frac{R_f (1 + \sin \theta)}{\cos \theta} . \tag{22}$$

Substituting Eq. (22) back into Eq. (18), we find a relation between contact angle θ and the maximum value of C,

$$C_{max} = \frac{\cos^2 \theta}{2}. (23)$$

The relations expressed by Eq. (22) is plotted in Fig. 4 (b), and Eq. (23) is plotted in the insert of Fig. 4 (b).

We notice that Eq. (22) specifies the radius of unduloidal drop having the contact angle with the fiber equal to the inflection angle of an unduloid[41, 42]. In other words, when $C=C_{max}$, the fiber radius R_f and the radius R_{inf} of the point where the curvature of the generator changes its sign coincide. Carrol conjectured that when $R_f=R_{inf}$, an unduloidal drop should be unstable and would turn into a clamshell[22]. The relation between R_{inf} and θ was later corrected by McHale's group[23, 43].

Thus, the area bounded by the dashed and dash-dotted curves in Fig. 4(b), corresponds to the unduloidal droplets with ascending C in Fig. 4(a). The unduloidal droplets with larger radii, including the infinitely large spherical droplet, sit above the dashed curve. Moreover, the dashed curve is the inflection point condition for an unduloidal drop: the droplets with radii greater than the dashed boundary will always contain a meniscus where the curvature changes its sign. The sign of the curvature of smaller droplets sitting below the dashed curve remains the same.

We further plot the dimensionless capillary pressure $\frac{\Delta PR_f}{\sigma}$ as a function of the ratio $\frac{R_{max}}{R_f}$, Fig. 4(c). This dependence appears monotonous. Therefore, we can re-parametrize C as a function of dimensionless capillary pressure $\frac{\Delta PR_f}{\sigma}$. This dependence $C(\frac{\Delta PR_f}{\sigma})$ is shown in Fig. 4(d). In both graphs, Fig. 4(c) - (d), the capillary pressure approaches zero when R_{max} goes to infinity.

2.6 Profile and volume of unduloidal drop

To find the unduloid profile, we rewrite Eq. (6) in the form

$$\frac{dy}{dx} = \cot \gamma \Rightarrow \frac{dx}{dy} = \tan \gamma = -\sin \gamma \left(1 - \sin^2 \gamma\right)^{-\frac{1}{2}} . \tag{24}$$

Using the first integral, $\sin \gamma = \frac{\Delta P}{2\sigma} y + \frac{C\sigma}{\Delta P} \frac{1}{y}$, we then obtain

$$\frac{dx}{dy} = -\left(\frac{\Delta P}{2\sigma}y + \frac{C}{\sigma} \cdot \frac{1}{y}\right) \left[1 - \left(\left(\frac{\Delta P}{2\sigma}y + \frac{C}{\sigma} \cdot \frac{1}{y}\right)\right)^{2}\right]^{-\frac{1}{2}} . \tag{25}$$

where C is defined by Eq. (18) and ΔP is defined by Eq. (16). The differential equation (25) can be numerically integrated from R_f to R_{max} using MATLAB ODE45 to provide the droplet shape, Fig. 5(a).

Hence, we can use MATLAB to integrate the function x(y) of the unduloid and to get its volume.

$$V = 2\pi \int_{R_f}^{R_{max}} y^2 \frac{dx}{dy} dy - 2\pi R_f^2 (x_{right} - x_{left}), \qquad (26)$$

where x_{left} and x_{right} are positions of the left and right contact lines.

Thus, by varying the drop size R_{max} from $\frac{R_f}{\cos\theta}$ to infinity, we can calculate the volume of unduloidal drops at any specific contact angle θ . Figure 5 (b) shows how the volume of an unduloidal drop changes. Again, the hollow triangles label the points where C reaches its maximum peak value corresponding to the inflection point criterion, and the asterisks correspond to the spherical drop forming the given contact angle with the fiber.

Using the algorithm explained in the Supplementary material, we numerically obtained a series of unduloids of fixed volume with different contact angles, Fig. 5(c).

The relation between the capillary pressure and unduloid volume is plotted in Fig. 5 (c). The smallest unduloid is a spherical drop (see asterisks in Fig. 5), with a maximum capillary pressure $2\sigma\cos\theta/R_f$. The capillary pressure decreases monotonously with an increase in the drop size.

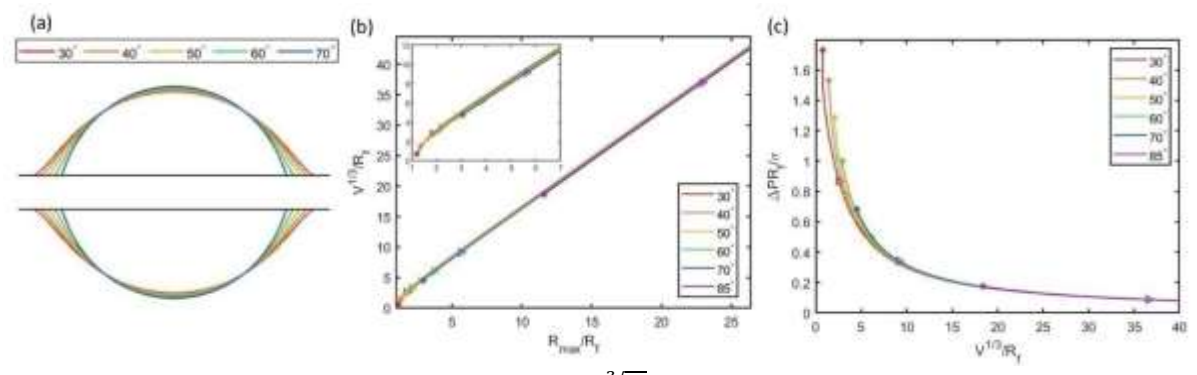


Fig. 5. (a) Unduloidal droplets of constant volume $\frac{\sqrt[3]{V_0}}{R_f}=0.0144$ making different contact angles with the fiber. (b) The dimensionless volume of an unduloidal drop plotted as a function of dimensionless drop radius. The insert shows this dependence for smaller R_{max}/R_f ratios. No

unduloidal drops of volume $\frac{\sqrt[3]{V_0}}{R_f}$ > 40 making 85° with the fiber exist. (c) Dimensionless capillary pressure versus dimensionless drop volume.

2.7 Nodoidal droplets

Consider a nodoidal drop sitting on a fiber of radius R_f . The drop forms a contact angle θ with the fiber surface, Fig. 3(f).

At the neck of the nodoid (point A in Fig. 3(f)), we have $\gamma=-\frac{\pi}{2}$ and $y=R_{min}$. Therefore, Eq. (10) is written as

$$-R_{min} = \frac{\Delta P}{2\sigma} R_{min}^2 + \frac{\sigma}{\Delta P} C. \tag{27}$$

At the bulge of the nodoid (point B in Fig. 3(f)), we have $\gamma = \frac{\pi}{2}$ and $y = R_{max}$. Then,

$$R_{max} = \frac{\Delta P}{2\sigma} R_{max}^2 + \frac{\sigma}{\Delta P} C. \tag{28}$$

Solving these two equations (27) - (28) for the pressure drop ΔP and C separately, we obtain

$$\Delta P = \frac{2\sigma}{R_{max} - R_{min}}. (29)$$

$$C = -\frac{2R_{max} R_{min}}{(R_{max} - R_{min})^2}. (30)$$

Comparing (13) with (29), one observes that the unduloidal drop of radius R_{max} will always have smaller capillary pressure than that of a nodoidal drop of the same R_{max} . The capillary pressure in nodoidal drop is still positive, i.e. the pressure in the nodoidal drop is greater than the pressure in the surrounding fluid.

2.8 Parameters of nodoidal drop on a fiber

To specify the nodoidal droplet, we must relate R_{min} with the fiber radius and droplet contact angle θ . At the contact line between nodoidal drop and the fiber (point C in Fig. 3(f)), we have $\gamma = \frac{\pi}{2} - \theta$ at $y = R_f$. Therefore,

$$R_f \sin\left(\frac{\pi}{2} - \theta\right) = \frac{\Delta P}{2\sigma} R_f^2 + \frac{\sigma}{\Delta P} C. \tag{31}$$

Using (28) to eliminate C, we obtain from (31):

$$\Delta P = 2\sigma \frac{R_{max} - R_f \cos \theta}{R_{max}^2 - R_f^2} \quad . \tag{32}$$

Then, using the pair of equations (27) and (31) to eliminate C, and Eq. (32) to express ΔP via R_{max} , we find

$$R_{\min} = \frac{R_f (R_{max} \cos \theta - R_f)}{R_f \cos \theta - R_{max}}.$$
 (33)

Similarly, C is found as,

$$C = \frac{R_{max}R_f(R_f\cos\theta - R_{max})(R_f - R_{max}\cos\theta)}{(R_f^2 - R_{max}^2)^2} . \tag{34}$$

2.9 Parametric analysis of the nodoidal droplets

In order to ensure the existence of a nodoidal drop on a fiber, we have to satisfy the following conditions:

- 1) The neck radius of the nodoid must be positive and smaller than the fiber radius.
- The bulge of nodoid must be located above the fiber's surface.
- 3) The contact angle θ is allowed to change from 0° degrees to 180° , $-1 \le \cos \theta \le 1$.

As proved in Supplementary material, for the given contact angle θ that varies from 0° to 90° degrees, a nodoidal drop could have its maximum radius R_{max} within the boundaries $R_f < R_{max} \le \frac{R_f}{\cos \theta}$. For contact angles within the range $90^\circ < \theta \le 180^\circ$, no restriction on R_{max} exists. In contrast to the unduloidal droplets, the constant C of nodoidal droplets is a monotonous function of n (see the proof in Supplementary material and the insert in Fig. 6 (c)).

Substituting C, Eq. (34), and ΔP , Eq. (32), into differential equation (25), the profile of nodoidal droplet x(y) is obtained numerically by integrating this differential equation from R_f to R_{max} using MATLAB ODE45, Fig. 6 (a-b); the volume of nodoidal drop is calculated using Eq. (26). Following the same algorithm for finding the droplets of equal volume (Supplementary materials, S2), we plot the profiles of nodoidal droplets forming different contact angles with the fiber, Fig. 6(a). This set of nodoidoidal droplets is obtained by first searching for a spherical drop with the radius $\frac{R_f}{cos\,\theta}$ and contact angles $\theta < 90^\circ$. For example, when $\theta = 61.75^\circ$, the corresponding dimensionless volume is equal to 3 and this limiting droplet is shown by the dashed line in Fig. 6 (a).

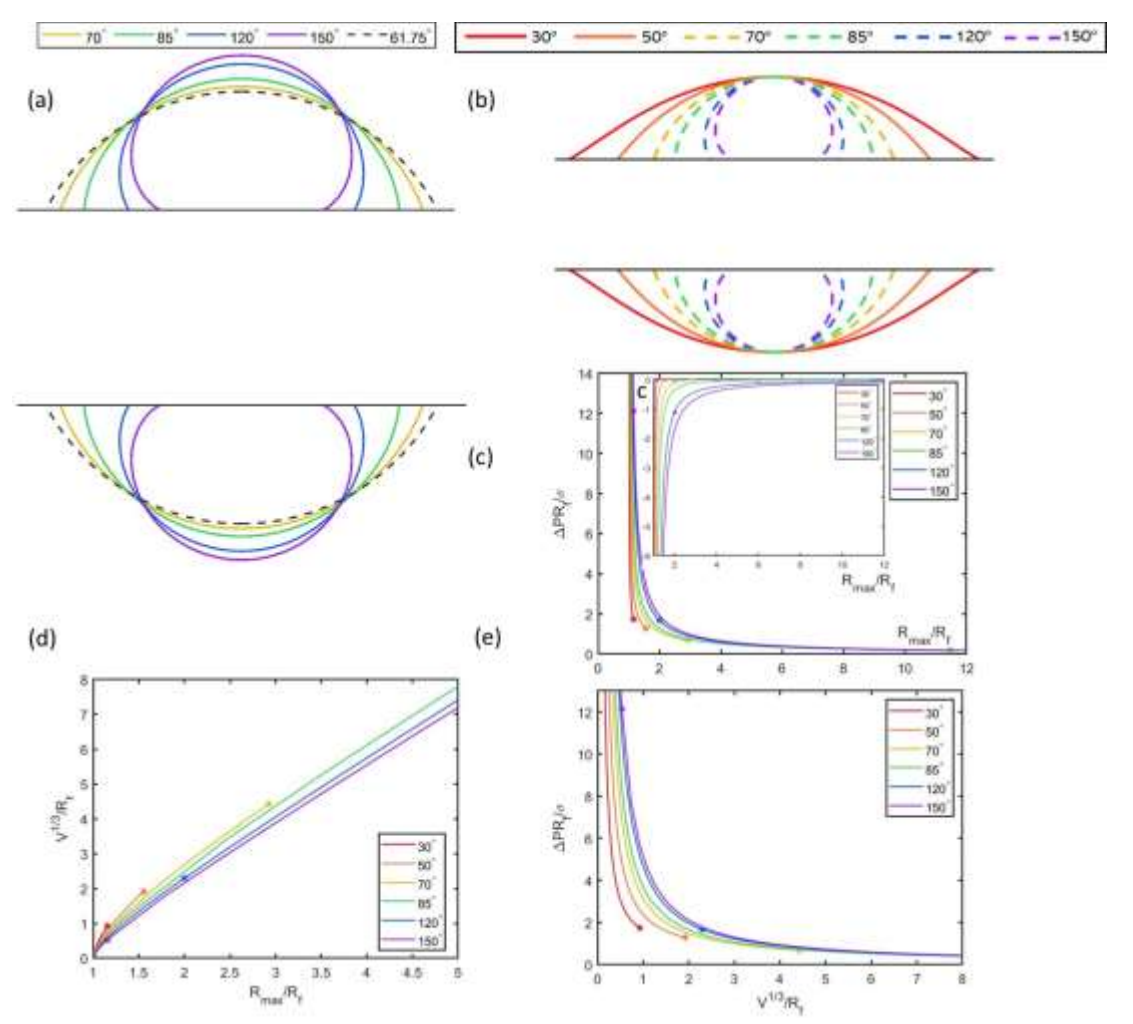


Fig. 6. (a) Nodoidal droplets of the same volume cannot make arbitrarily chosen contact angles with the fibers. In this example of droplets of dimensionless volume equal to 3, no nodoidal droplets making 30° or 50° with the fiber exist. The black dashed line shows the profile of a nodoidal drop having the smallest possible contact angle 61.75° among the drops of the same volume. (b) A series of nodoidal and unduloidal droplets with different volumes having constant R_{max}/R_f and making different contact angles with the fiber. The dashed curves show nodoidal droplets, while the solid curves show the unduloidal drops of the same dimensionless radius making 30° and 50° degrees contact angle with the fiber when no nodoidal droplets exist. (c)

Dimensionless capillary pressure $\frac{\Delta PR_f}{\sigma}$ versus dimensionless radius of nodoidal drop $\frac{R_{max}}{R_f}$. The asterisks in this series of graphs correspond to $R_{max} = \left| \frac{R_f}{\cos \theta} \right|$. Notice that though the ratio $\left| \frac{R_f}{\cos \theta} \right|$ for $\theta = 30^\circ$ and 150° is the same, the capillary pressure $\Delta P = 2\sigma \frac{R_{max} - R_f \cos \theta}{R_{max}^2 - R_f^2}$ is different because of the different signs of cosine. The insert shows the dependence of constant C on R_{max}/R_f for nodoidal droplets making different contact angles with the fiber. In contrast to unduloidal droplets, this dependence is always monotonous. The asterisks correspond to $R_{max} = \left| \frac{R_f}{\cos \theta} \right|$. (d) Dimensionless volume of nodoidal droplets as a function of R_{max}/R_f . The asterisk corresponding to the spherical drop having the 85° contact angle is out of range $(\frac{V^{\frac{1}{3}}}{R_f} > 8)$. (e) Dimensionless capillary pressure $\frac{\Delta PR_f}{\sigma}$ versus dimensionless volume $V^{\frac{1}{3}}/R_f$. The asterisk corresponding to the spherical drop having the 85° contact angle is out of range $(\frac{V^{\frac{1}{3}}}{R_f} > 8)$.

The dimensionless capillary pressure of nodoidal drop $\frac{\Delta PR_f}{\sigma}$ decreases monotonously from infinity to $2\cos\theta$ when R_{max} increases from R_f to infinity, Fig. 6(c).

The volume of nodoidal droplets as a function of the dimensionless radius of the drop is shown in Fig. 6(d).

The relation between the capillary pressure and volume of nodoidal droplet is plotted in Fig. 6 (e). The asterisks correspond to the droplets with $R_{max}=\left|\frac{R_f}{\cos\theta}\right|$ with capillary pressure

$$\Delta P = \begin{cases} \frac{2\sigma\cos\theta}{R_f} & (0^{\circ} < \theta < 90^{\circ}) \\ 2\sigma\frac{R_{max} - R_f\cos\theta}{R_{max}^2 - R_f^2} & (90^{\circ} < \theta < 180^{\circ}) \end{cases}$$
(35)

The capillary pressure decreases monotonously with the drop size.

2.9 Transition between unduloids and nodoids

As shown, nodoidal and unduloidal droplets represent two families of axisymmetric droplets that could potentially rest on the fibers. Figure 7 (a) shows the relations between the dimensionless capillary pressure and dimensionless drop volumes for these solutions at the fixed contact angles specified by different colors. The solid curves represent unduloidal droplets, and the dashed curves represent nodoidal droplets. In unduloidal droplets, two markers indicate two limiting cases. The asterisks mark limiting spherical drops; the hollow triangles correspond to the drop with an inflection point at the contact line, i.e., the point where the unduloidal drop has a maximum value of \mathcal{C} .

As expected, the curves for unduloidal and nodoidal droplets merge when these two solutions approach their shared spherical drop with radius $R_{max}=R_{\phi}=R_f/\cos\theta$. The continuity of curves in Fig. 7(a) indicates that the nodoidal droplets could spontaneously transform into the unduloidal droplet when the droplet volume increases above the limiting volume corresponding to the volume of the limiting spherical droplet.

Accordingly, the capillary pressure of smaller nodoidal droplets is always greater than that of the larger unduloidal droplets.

We further analyze the surface energy of unduloids and nodoids. The surface energy, W, of a drop on the fiber includes two parts: 1) interfacial energy between the drop and surrounding fluid, $W_1 = \sigma A_{drop}$, where A_{drop} is the surface area of the drop. 2) The work of adhesion between drop and fiber, $W_2 = \sigma(1+\cos\theta)A_{fiber}$, where A_{fiber} is the wetted area of the fiber under the drop.

The surface area A_{drop} is determined by integrating the following equation,

$$A_{drop} = 4\pi \int_{R_f}^{R_{max}} y \frac{ds}{dy} dy$$
 (36)

The wetted area of the fiber under the drop is calculated as

$$A_{fiber} = 2\pi R_f L \tag{37}$$

Where the wetted length L is obtained by integration of Eq. (25): $L=2(x_1-x_0)$ where

$$x = \begin{cases} x_0(y = R_f) \\ x_1(y = R_{max}) \end{cases}$$

Thus, the surface energy of droplets is calculated as

$$W = W_1 + W_2 = 4\sigma\pi \int_{R_f}^{R_{max}} y \frac{ds}{dy} dy + 2\sigma\pi R_f L(1 + \cos\theta)$$
 (38)

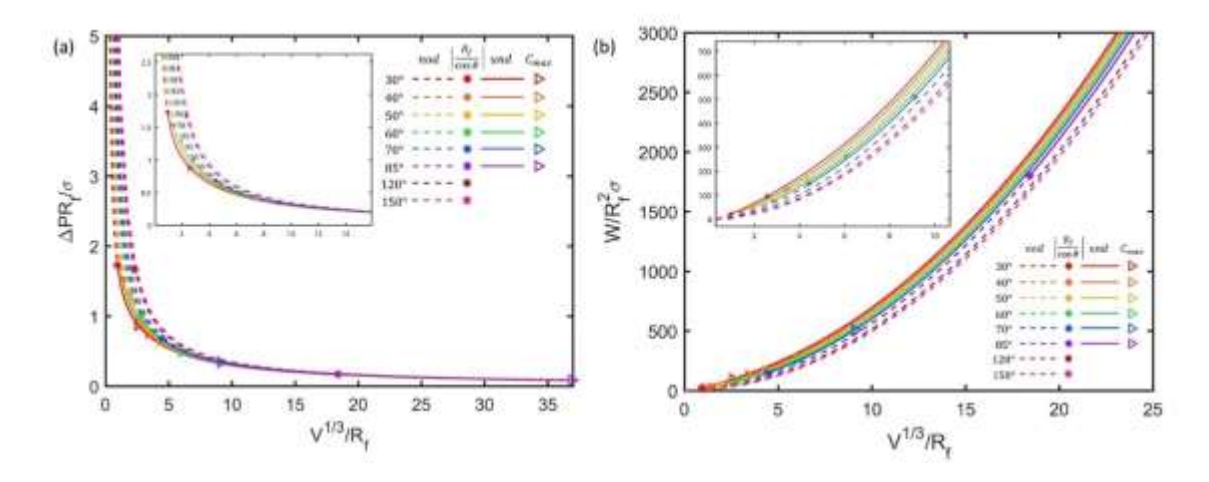


Fig. 7. (a) Dimensionless capillary pressure $\frac{\Delta PR_f}{\sigma}$ of unduloidal and nodoidal droplets versus dimensionless volume $V^{\frac{1}{3}}/R_f$. (b) Dimensionless surface energy $\frac{W}{R_f^2\sigma}$ of unduloidal and nodoidal droplets versus dimensionless volume $V^{\frac{1}{3}}/R_f$.

In Fig. 7(b), we plot the dimensionless surface energy $\frac{W}{R_f^2\sigma}$ of unduloidal and nodoidal droplets as a function of their dimensionless volume $\frac{V^{\frac{1}{3}}}{R_f}$. The comparison of this energy makes sense only for the wetting case when the contact angle is less than 90°. The dashed lines always appear before the solid lines, meaning that the surface energy of the nodoidal droplet is always smaller. Therefore, the smaller droplets are always nodoidal. Then, increasing the drop volume, the nodoidal drop transforms into an unduloidal drop. The energies of these two configurations with the same volume are equal only for limiting spherical droplets.

3 Experimental validation of the existence of nodoidal droplets

These experiments aim to confirm the existence of an equilibrium nodoidal drop with an inverted meniscus making a contact angle greater than 90° with a fiber. Experiments on hundred-micrometer fibers show that an unsupported barreled drop is unstable at large contact angles: it transforms into a clamshell drop[8, 18, 19, 21-26]. In experiments, the observed barreled droplets were unduloidal, and their transformation to clamshells followed the inflection point criterion. Thus, the inflection point criterion serves as an indicator for the barrel-clamshell transition. In these experiments, the clamshells were small, and the fibers were large enough to support them. We question: "What will happen when tens or hundreds of micrometers aerosol drops hit submicrometer fibers?" Will non-wettable fiber support axisymmetric drops? To the best of our knowledge, no systematic analysis of this scenario when the drop is supposed to take on a nodoidal shape has been done so far. It is unclear whether any experimental limitation on the fiber diameter and drop size exists to observe these droplets. Therefore, it is too early to state that the clamshells are the only stable configuration for large contact angles.

To illustrate the challenges associated with analyses of interactions of droplets with fine fibers, we used hydrophobic Basalt fibers (FibreCoat GmbH) of 21 microns in diameter. As shown in the Supplementary material, the advancing contact angle that water makes with the fiber is greater than 90° and the receding contact angle is 56° .

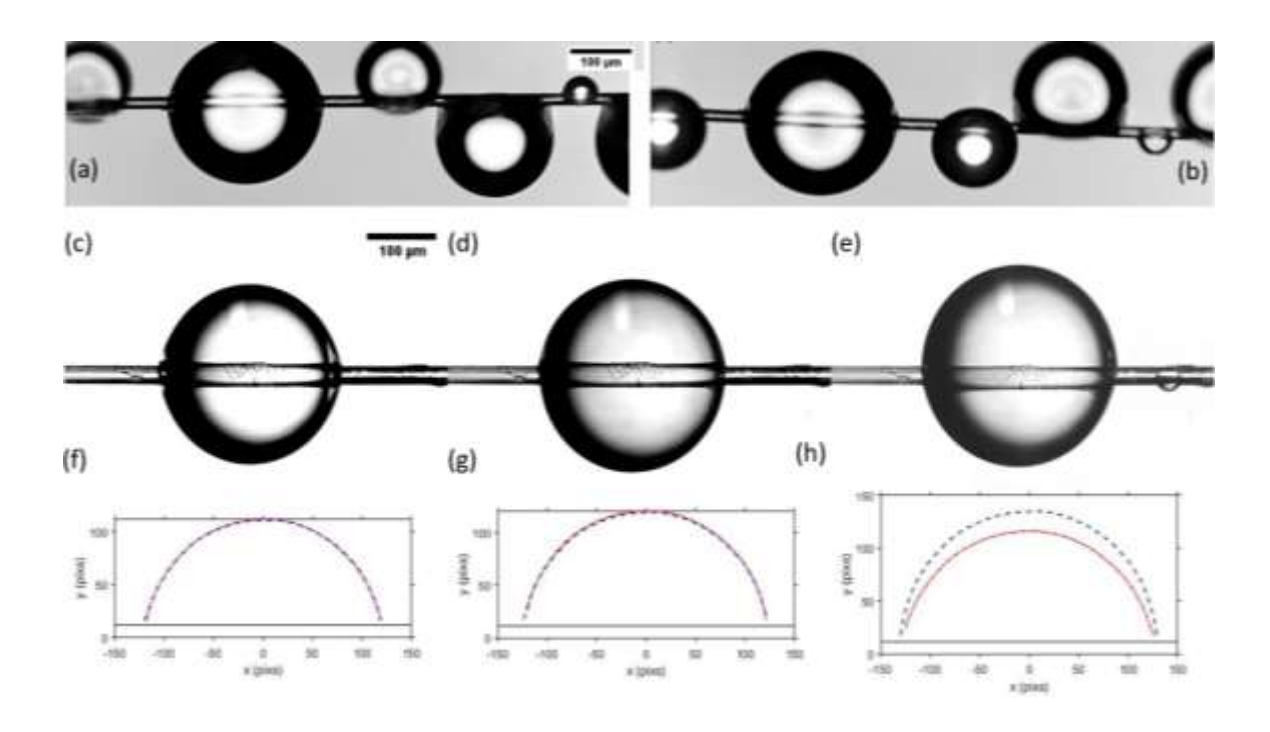


Fig. 8. (a) Water droplets sprayed on the Basalt fiber. Notice that the barreled droplets are not axisymmetric. (b) To confirm that gravity is insignificant, the fiber was 180° rotated around the fiber axis to flip the top and bottom sides of the drops in (a). Neither barreled droplets nor clamshell droplets fall: the bigger bulge from the bottom was safely moved to the top, confirming that gravity is insignificant. (c)-(e) An axisymmetric unduloidal drop was increased in size by spraying more water droplets on it. It eventually turned into a nonsymmetric drop. (f)-(h) The profiles of the upper and lower parts of the droplets extracted with an edge detection LabView program "IMAQ Extract Contour VI".

On these fibers, the water droplets could take on barreled and clamshell shapes, Fig. 8 (a)-(b). The droplet weight is insignificant: this is proved by rotating the fiber by180° about its axis and confirming that the droplets do not change their shape. The noticeable asymmetry of the barreled droplets is, probably, caused by the contact angle hysteresis,

as explained below. To probe the droplet shape when the contact lines advance over dry parts of the fiber, we prepared an unduloidal droplet shown in Fig. 8(c). The upper and lower parts of the extracted profile are best fitted with two surface patches of unduloidal drops, the upper making $\theta=76.7^{\circ}$ and the lower making $\theta=76.2^{\circ}$ contact angles with the fiber. Within the acceptable experimental error, these angles are very close one to the other, confirming that the drop has an unduloidal shape.

After spraying more water on it, this unduloidal droplet kept its unduloidal shape, Fig. 8(d): the upper and lower unduloidal surface patches meet the fiber at almost the same contact angles, the upper making 82.8°, and the lower making 82.5° contact angles with the fiber. A noticeable increase in the advancing contact angle suggests that the end menisci meet the drier parts of the fiber relative to those in Fig. 8(c).

The drop suddenly lost its symmetry after spraying more water on it, Fig. 8(e). The upper side of the drop bulges stronger than the lower side. The upper and lower parts of the extracted profile cannot be fitted with two surface patches of unduloidal drops. The best trial function for fitting the upper part appeared to be nodoidal patch making $\theta=92.3^{\circ}$ contact angle with the fiber and the best trial function for fitting the lower part appeared to be unduloidal patch making $\theta=62.9^{\circ}$ contact angle with the fiber. It is understandable that nonsymmetric drop cannot be described by nodoidal or unduloidal shapes, but this fitting indicates a trend toward achieving a shape resembling a nodoidal drop when the drop volume increases. We were not able to obtain axisymmetric nodoidal

droplets by spraying more water: the upper part remained larger until the drop fell down under its own weight.

These experiments illustrate the difficulty of working with micrometer-sized fibers and droplets: at this scale, the contact angle hysteresis significantly affects the droplet shape[44]. We, therefore, turned to another experimental setup that mimics the drop behavior at smaller scales and, at the same time, allows us to work with available fibers.

Instead of spraying droplets on fibers, we "pierced" a hemispherical droplet resting at the end of a capillary tube. These experimental conditions fully satisfy the boundary conditions of the model.

As schematically illustrated in Fig. 9, a drop of water is slowly formed at the end of a capillary tube. The fiber was coaligned with the tube axis, and when the drop was released, the fiber remained partly inserted inside the tube. When the drop diameter becomes equal to the tube diameter, the drop approaches the end of the capillary tube horizontally with the slope parallel to the tube axis. This drop mimics one-half of a free-standing drop on a fiber with the same boundary condition at the equator. According to the model and results presented in Fig. 6(d), changing the contact angle at fixed R_{max}/R_f , one changes the drop volume.

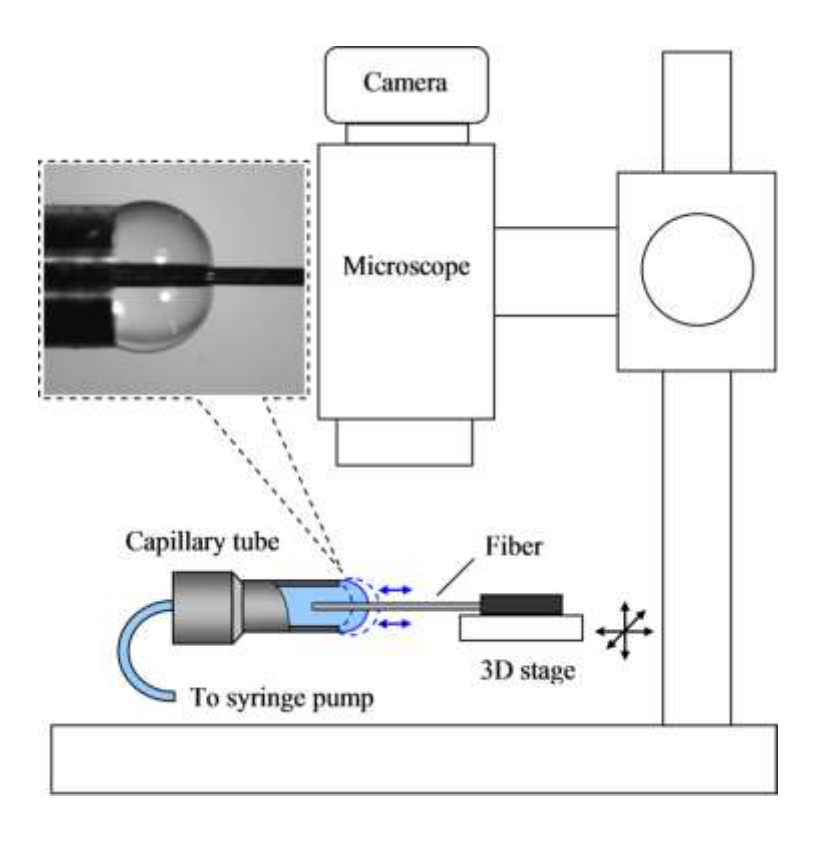


Fig. 9. Experimental setup allowing to validate the models of axisymmetric droplets on fibers. A syringe pump allowing the user to control the drop volume is connected to a capillary tube. A fiber coaligned with the tube axis by a 3D stage is partially inserted in the tube. The tube-fiber system is placed under the microscope, and the process of drop release and its evaporation is filmed with a camera. The drop profiles at different time moments are shown as dashed lines. The solid line selects a hemispherical drop of interest.

As a capillary tube, we used a 20G medical needle with an outer diameter of $2R=1.27\ mm$. A stainless-steel rod of $2R_f=0.170mm$ in diameter was used as a fiber. The tip of the needle was cut and polished. Thus $R_{max}=R=0.635\ mm$, and $R_{max}/R_f=7.47$. The rod was coated with a thin layer of microcrystalline wax (Cosmoloid H80, Kremer Pigmente GmbH). The measured static contact angle of DI water on the wax was

 $\theta=103^{\circ}\pm2^{\circ}$. The effect of gravity on the drop shape was negligible as proved by the estimated Bond number $Bo=\frac{R_{max}^{2}\rho g}{\sigma}=0.028\ll1$. All the experiments were performed under ambient conditions (22°C-25°C).

The advancing contact angles were studied by extruding/withdrawing DI water at a controlled rate. Extruding water at the rate 0.014mm³/s and tracking the contact line movement, its velocity U=0.0076 mm/s was estimated at the moment when the droplet radius reached the needle radius $R=R_{max}$. This velocity was repeatable from one experiment to the other. The receding contact angle was also investigated by tracing the movement of the evaporating meniscus. During evaporation, the same condition $R=R_{max}$ was achieved at different velocities ranging from 0.00017 to 0.00045 mm/s. In all cases, the capillary number $Ca=\frac{U\eta}{\sigma}\sim O(10^{-9})-O(10^{-7})$, (η is the water viscosity), was very much smaller than 1, indicating that the capillary forces control the drop shaping. Therefore, we consider the droplets to be in a quasi-equilibrium state.

The photographs of the drops and the results of their fitted profiles are presented in Fig. 10. We confirmed that the water drop on the hydrophobic rod takes on an apple-like shape with the inverted meniscus forming the contact angle θ =100.5±1.4° (average ± standard deviation based on five experiments). Therefore, within experimental error, the best-fit profile recovers the measured contact angle. The droplet is nodoidal, indeed.

When water was slowly withdrawn from the droplet, the nodoidal droplet was transformed into an unduloidal droplet with the θ =56.2° contact angle.

The above experiments confirm the existence of a nodoidal drop on a fiber. They also demonstrate the possibility of changing the droplet shape by moving the fiber in and out from the drop.

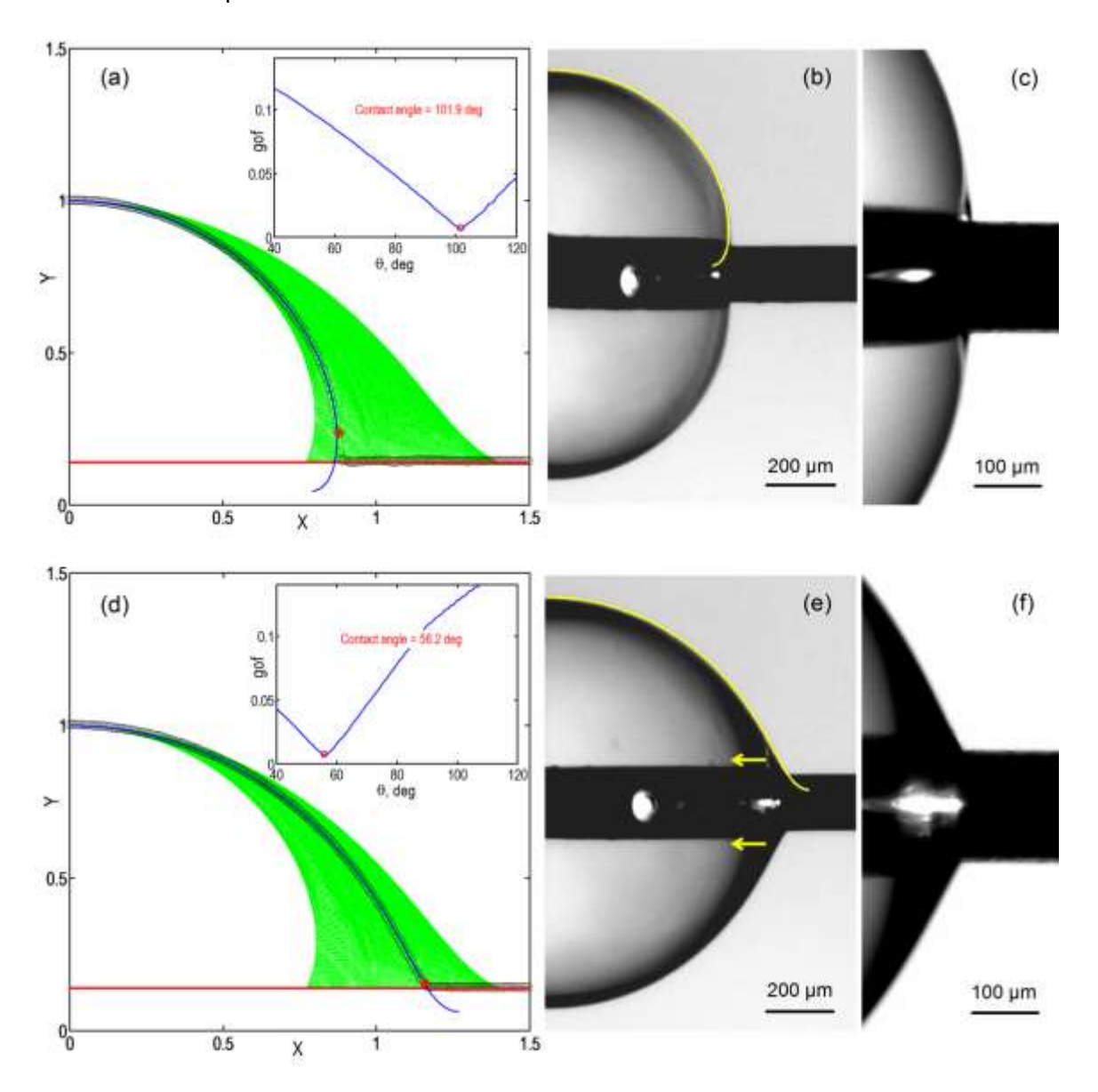


Fig. 10. (a-c) A quasi-equilibrium configuration of the droplet: (a) Illustration of the output of the fitting algorithm. The drop profile was normalized by the maximum radius of the drop, R_{max} . The

open dots mark the experimental profile (only every other experimental point is shown, and the last fitted point is asterisked); the red horizontal line is the rod surface; the green area is filled with the set of theoretical profiles used for searching the best fit by changing contact angles; the blue line is the best-fit nodoidal profile ($\theta = 101.9^{\circ}$). The inset: the goodness of fit (gof, Supplementary materials, S4) versus contact angle; the smallest gof is achieved when a nodoidal function describes the drop profile with θ =101.9°. (b) The top view of a water drop with the overlaid best-fit nodoidal profile (the yellow line). (c) The photograph was taken at the 80° angle with respect to the rod axis to make the inverted meniscus visible. (d-f) A dynamic configuration of the droplet: the contact line recedes with the 0.00017mm/s velocity due to the drop evaporation; the best-fit unduloidal profile makes the θ =56.2° contact angle with the rod.

4 Conclusions

The complete classification of axisymmetric shapes of droplets on fibers has been provided for the no-gravity case. In our theory, the wetting properties of fibers were varied to cover the entire range of contact angles, from 0° to 180° . The shapes of these droplets are described by the Laplace equation of capillarity, a non-linear second-order differential equation with very special boundary conditions. This problem can be analyzed using the phase portrait shown in Fig. 3(a-b). It is shown that the droplets could take on only two possible shapes described by unduloidal or nodoidal surface patches of the two constant-mean curvature surfaces.

When the contact angle θ that the drop makes with the fiber of radius R_f is less than 90° , the axisymmetric droplet could be either unduloidal or nodoidal. A nodoidal drop could have its maximum radius R_{max} within the boundaries $R_f < R_{max} \le \frac{R_f}{\cos \theta}$. In contrast, unduloidal droplets with the same contact angle should have larger maximum radius varying within the range $\frac{R_f}{\cos \theta} < R_{max} < \infty$. A spherical droplet of radius $R_{max} = R_{\emptyset} = \frac{R_f}{\cos \theta}$ separates these two configurations. The transition from one configuration to the other is monotonous with respect to the drop volume and capillary pressure.

Unduloidal droplets of maximum radius $R_{max} = \frac{R_f(1+\sin\theta)}{\cos\theta}$ have very special geometrical meaning: these droplets meet the fiber at the inflection points on their profile[23]. This special property directly follows from the parametric analysis of unduloidal solutions, Eqs(21)-(23), and is illustrated in Fig. 4.

An analysis of the free energy of these two types of droplets reveals that the surface energy of the nodoidal droplet is always smaller than the energy of unduloidal droplets. Thus, the smaller axisymmetrical droplets are always nodoidal, which transforms into unduloidal droplets with an increase in the drop volume. The energies of these two configurations with the same volume are equal only for limiting spherical droplets of radius $R_{\emptyset} = \frac{R_f}{\cos \theta}$.

When the contact angle θ is greater than 90° , only nodoidal axisymmetric droplets could exist.

A series of experiments with free-standing droplets obtained by spraying water on fibers showed that the barreled droplets with a contact angle greater than 90° could be formed on these fibers. However, we could not obtain axisymmetric droplets: most likely, the contact angle hysteresis significantly influences the drop formation process. We, therefore, turned to a setup where only one contact angle determines the droplet shape. By forming a hemispherical drop at the end of a capillary tube and piercing the drop with fiber, we were able to satisfy all the boundary conditions required by the Laplace model. It was confirmed that the nodoidal apple-like droplets could be repeatably formed. Fixing the ratio R_{max}/R_f , and withdrawing the fiber from the nodoidal drop, we confirmed that an unduloidal drop could be formed and its receding contact angle satisfies the theoretically derived condition: $\cos\theta < \frac{R_f}{R_{max}}$.

The obtained results complete the classification of morphological configurations of axisymmetric droplets on fibers and could be used in many applications in fiber science and biology [1-6, 45, 46], where one needs to evaluate the possibility of obtaining axisymmetric droplets on fibers. The developed theory significantly enriches the existing scenario of the formation of drops on fibers by introducing nodoidal solutions of the Laplace equation of capillarity. We believe that with the developments in nanotechnology and nanofluidics [47-49], where gravity is not significant, or in space exploration applications, this theory will be helpful for the design of fluidic devices and fluid management with fibrous materials [17, 50-53].

Supplementary material

This material includes the details on the solution of Eq.(21), an explanation of the numeric algorithm for calculating unduloidal and nodoidal droplets of the same volume with more examples, derivation and analyses of conditions for the existence of nodoidal droplets, and protocol for fitting the drop profile.

ACKNOWLEDGMENTS

Y.S. and K.G.K. are partially supported by the NSF grant IOS 2014664. A.V.B. is partially supported by the Government program (Project 123021700044-0).

DATA AVAILABILITY

The data that supports the findings of this study are available within the article and its supplementary material.

REFERENCES

- [1] B.D. Opell, D. Jain, A. Dhinojwala, T.A. Blackledge, Tuning orb spider glycoprotein glue performance to habitat humidity, Journal of Experimental Biology 221(6) (2018). [2] H. Bai, J. Ju, Y.M. Zheng, L. Jiang, Functional Fibers with Unique Wettability Inspired
- by Spider Silks, Advanced Materials 24(20) (2012) 2786-2791.
- [3] Y.M. Zheng, H. Bai, Z.B. Huang, X.L. Tian, F.Q. Nie, Y. Zhao, J. Zhai, L. Jiang, Directional water collection on wetted spider silk, Nature 463(7281) (2010) 640-643.
 - [4] G.W. Koch, S.C. Sillett, G.M. Jennings, S.D. Davis, The limits to tree height, Nature 428(6985) (2004) 851-854.
- [5] T.E. Dawson, G.R. Goldsmith, The value of wet leaves, New Phytologist 219(4) (2018) 1156-1169.

- [6] S.G. Gotsch, N. Nadkarni, A. Darby, A. Glunk, M. Dix, K. Davidson, T.E. Dawson, Life in the treetops: ecophysiological strategies of canopy epiphytes in a tropical montane cloud forest, Ecological Monographs 85(3) (2015) 393-412.
 - [7] Y. Sun, J. Ma, F. Peng, K.G. Kornev, Making droplets from highly viscous liquids by pushing a wire through a tube, Physics of Fluids 34(3) (2022).
- [8] H.B. Eral, J. de Ruiter, R. de Ruiter, J.M. Oh, C. Semprebon, M. Brinkmann, F. Mugele, Drops on functional fibers: from barrels to clamshells and back, Soft Matter 7(11) (2011) 5138-5143.
 - [9] A. Ghosh, D. Bandyopadhyay, A. Sharma, Micro-patterning of coatings on a fiber surface exploiting the contact instabilities of thin viscoelastic films, Physics of Fluids 30(11) (2018).
 - [10] K. Keis, K.G. Kornev, Y.K. Kamath, A.V. Neimark, Towards Fiber-Based Micro- and Nanofluidics,, in: S. Guceri, Y.G. Gogotsi, V. Kuznetsov (Eds.), Nanoengineered Nanofibrous Materials, NATO Science Series II: Mathematics, Physics and Chemistry, Kluwer Publishing, New York, 2004, pp. 175-182.
 - [11] A. Marmur, Measures of wettability of solid surfaces, European Physical Journal-Special Topics 197(1) (2011) 193-198.
- [12] A. Marmur, C. Della Volpe, S. Siboni, A. Amirfazli, J.W. Drelich, Contact angles and wettability: towards common and accurate terminology, Surface Innovations 5(1) (2017) 3-8.
 - [13] P.-G. Gennes, F. Brochard-Wyart, D. Quéré, Capillarity and Wetting Phenomena: Drops, Bubbles, Pearls, Waves, Springer, New York, 2004.
 - [14] D. Bonn, J. Eggers, J. Indekeu, J. Meunier, E. Rolley, Wetting and spreading, Rev. Mod. Phys. 81(2) (2009) 739-805.
 - [15] A.B.D. Cassie, Physics and textiles, Reports on Progress in Physics 10 (1945) 141-171.
- [16] B. Miller, The wetting of fibers, in: M.J. Schick (Ed.), Surface characteristics of fibers and textiles, Marcel Dekker, New York, 1977, pp. 417-445.
- [17] C. Duprat, Moisture in Textiles, Annual Review of Fluid Mechanics 54 (2022) 443-467.
- [18] T.H. Chou, S.J. Hong, Y.E. Liang, H.K. Tsao, Y.J. Sheng, Equilibrium Phase Diagram of Drop-on-Fiber: Coexistent States and Gravity Effect, Langmuir 27(7) (2011) 3685-3692.
 [19] C.W. Xu, Z.Y. Lu, L.R. Li, Surface Evolver Simulation of Droplet Wetting Morphologies on Fiber Without Gravity, Frontiers in Energy Research 9 (2022).
 - [20] A. Gupta, A.R. Konicek, M.A. King, A. Iqtidar, M.S. Yeganeh, H.A. Stone, Effect of gravity on the shape of a droplet on a fiber: Nearly axisymmetric profiles with experimental validation, Physical Review Fluids 6(6) (2021).
- [21] N.K. Adam, Detergent Action and its Relation to Wetting and Emulsification, Journal of the Society of Dyers and Colourists 53(4) (1937) 121-129.
- [22] B.J. Carroll, Equilibrium conformations of liquid drops on thin cylinders under forces of capillarity. A theory for the roll-up process, Langmuir 2(2) (1986) 248-250.

- [23] G. McHale, M.I. Newton, B.J. Carroll, The shape and stability of small liquid drops on fibers, Oil & Gas Science and Technology-Revue De L Institut Français Du Petrole 56(1) (2001) 47-54.
- [24] G. McHale, M.I. Newton, Global geometry and the equilibrium shapes of liquid drops on fibers, Colloids and Surfaces A: Physicochemical and Engineering Aspects 206 (2002) 79-86.
- [25] R. Rosso, E.G. Virga, General stability criterion for wetting, Physical Review E 68(1) (2003).
- [26] M. Brinkmann, J. Kierfeld, R. Lipowsky, A general stability criterion for droplets on structured substrates, Journal of Physics a-Mathematical and General 37(48) (2004) 11547-11573.
- [27] J. Plateau, Experimental and theoretical researches on the figures on equilibrium of a liquid mass withdrawn from the action of gravity, Annual Report of the Board of Regents of the Smithsonian Institution Smithsonian Institution, Washington, DC, 1863, pp. 207–285.
- [28] L. Rayleigh, On the Capillary Phenomena of Jets, Proceedings of The Royal Society of London 29 (1879) 71-97.
- [29] D.W. Thompson, On growth and form, Cambridge: University Press New York 1945.
- [30] D. Quere, Fluid coating on a fiber, Annual Review of Fluid Mechanics 31 (1999) 347-384.
- [31] B.D. Opell, Water harvesting during orb web recycling, Journal of Arachnology 48(3) (2020) 278-283.
- [32] S.D. Stellwagen, B.D. Opell, M.E. Clouse, The impact of UVB radiation on the glycoprotein glue of orb-weaving spider capture thread, Journal of Experimental Biology 218(17) (2015) 2675-2684.
- [33] G.K. Batchelor, An introduction to fluid dynamics, Cambridge University Press, New York, 2000.
- [34] R.W. Balluffi, S.M. Allen, W.C. Carter, R.A. Kemper, Kinetics of materials, J. Wiley & Sons, Hoboken, N.J., 2005.
- [35] B.J. Carroll, The Accurate Measurement of Contact-Angle, Phase Contact Areas, Drop Volume, and Laplace Excess Pressure in Drop-on-Fiber Systems, Journal of Colloid and Interface Science 57(3) (1976) 488-495.
 - [36] H.M. rincen, The equilibrium shape of interfaces, drops, and bubbles, in: E. Matijevic (Ed.), Surface and Colloid Science, Wiley, New York, 1969, pp. 1-84.
- [37] D.W. Langbein, Capillary Surfaces: Shape Stability Dynamics, in Particular Under Weightlessness Springer, New York, 2002.
 - [38] P.S. Laplace, Mecanique Celeste, Encyclopaedia Britannica, Paris, 1806.
- [39] A.W. Adamson, A.P. Gast, Physical chemistry of surfaces, Wiley, New York, 1997. [40] J.C. Maxwell, Capillary action, Encyclopaedia Britannica, 1875.
- [41] G. McHale, auml, N.A. b, M.I. Newton, S.M. Rowan, Wetting of a High-Energy Fiber Surface, J Colloid Interface Sci 186(2) (1997) 453-61.

- [42] S. Rebouillat, B. Letellier, B. Steffenino, Wettability of single fibres beyond the contact angle approach, Int. J. Adhes. Adhes. 19(4) (1999) 303-314.
- [43] A.V. Neimark, Thermodynamic equilibrium and stability of liquid films and droplets on fibers, Journal of Adhesion Science and Technology 13(10) (1999) 1137-1154.
- [44] Y. Sun, K.G. Kornev Does the contact angle hysteresis control the droplet shapes on cylindrical fibers?, Colloids and Surfaces A: Physicochemical and Engineering Aspects 668 (2023) 131435.
 - [45] K.G. Kornev , P.H. Adler, Physical determinants of fluid feeding in insects, in: H. Krenn (Ed.), Insect mouthparts- form, function, development and performance, Springer, New York, 2019, pp. 263-314.
 - [46] Y.P. Chen, Z.P. Zhu, M. Steinhart, S.N. Gorb, Bio-inspired adhesion control with liquids, Iscience 25(3) (2022).
- [47] M.P. Rossi, Y. Gogotsi, K.G. Kornev, Deformation of Carbon Nanotubes by Exposure to Water Vapor, Langmuir 25(5) (2009) 2804-2810.
 - [48] M.P. Rossi, H.H. Ye, Y. Gogotsi, S. Babu, P. Ndungu, J.C. Bradley, Environmental scanning electron microscopy study of water in carbon nanopipes, Nano Letters 4(5) (2004) 989-993.
- [49] D. Mattia, Y. Gogotsi, Review: static and dynamic behavior of liquids inside carbon nanotubes, Microfluidics and Nanofluidics 5(3) (2008) 289-305.
 - [50] D.H. Reneker, A.L. Yarin, Electrospinning jets and polymer nanofibers, Polymer 49(10) (2008) 2387-2425.
- [51] G.C. Rutledge, S.V. Fridrikh, Formation of fibers by electrospinning, Advanced Drug Delivery Reviews 59(14) (2007) 1384-1391.
- [52] A. Tuteja, W. Choi, M.L. Ma, J.M. Mabry, S.A. Mazzella, G.C. Rutledge, G.H. McKinley, R.E. Cohen, Designing superoleophobic surfaces, Science 318(5856) (2007) 1618-1622.
- [53] D.Y. Miao, N.B. Cheng, X.F. Wang, J.Y. Yu, B. Ding, Integration of Janus Wettability and Heat Conduction in Hierarchically Designed Textiles for All-Day Personal Radiative Cooling, Nano Letters 22(2) (2022) 680-687.